Synthetic Bandwidth Radar for Ultra-Wideband Microwave Imaging Systems

Yifan Wang, Amin Abbosh, *Senior Member IEEE*, Bassem Henin, and Phong Nguyen

Abstract — A synthetic bandwidth radar as an approach to build ultra-wideband (UWB) imaging systems is presented. The method provides an effective solution to mitigate the challenges of UWB antenna's implementation with ideal performance. The proposed method is implemented by dividing the utilized UWB into several channels, or sub-bands, and designing an antenna array that includes a number of antennas equal to the number of channels. Each of those antennas is designed to have ideal properties across its corresponding channel. As part of the proposed approach, a two-stage calibration procedure is used to accurately estimate the effective permittivity of a heterogeneous imaged object at different angles and the phase center of each antenna for accurate delay time estimation. When imaging an object, each of the antennas transmits and captures signals only at its channel. Those captured signals are properly combined and processed to form an image of the target that is better than the current systems that use array of UWB antennas. The presented method is tested on breast imaging using the band 3-10 GHz via simulations and measurements on a realistic heterogeneous phantom.

***Index Terms*— Microwave imaging, microwave antenna, ultra wideband, synthetic bandwidth.**

I. Introduction

Recent years have witnessed an increased interest in using wideband microwave techniques to obtain internal images of various dielectric objects [1]-[6]. One of the extensively researched areas is the ultra-wideband "breast radar" aiming at the detection of breast's tumor by using the band from around 3 GHz to 10 GHz [5], [6]. The traditional approach in those systems is to use an antenna or array of antennas that is designed to operate across the whole band of interest.

One of the critical components that decides the success, or otherwise, of UWB imaging systems is the antenna that couples the microwave signal from the transmitter into breast tissues [6]. The characteristics of the UWB antenna strongly influence the system's reliability and imaging resolution. To guarantee a high quality image, the utilized UWB antenna should: 1) have excellent impedance match, 2) have fixed phase center and distortion-less impulse response [7], 3) have constant transmit efficiency [8], 4) have frequency-independent radiation pattern, and 5) be compact in structure. However, it is challenging to design antennas that meet all those harsh requirements across more than 100% fractional bandwidth as needed by UWB imaging systems. Thus, the utilized antennas in UWB imaging systems are usually designed with compromised properties that act as microwave filters and distort the transient radar pulse [9]-[10]. Such weaknesses of antennas in the imaging system bring clutter within the resolution cell and lower the possibility of a successful detection of early tumors [11]. The tradeoffs that naturally exist among various antenna properties and their design limitations are summarized in [12].

To overcome the challenges in UWB antenna design, the synthetic bandwidth approach is presented. It divides the utilized UWB in several channels. An antenna is then designed to operate in one of those channels. The scattered signals from the imaged object at all the channels are then properly combined and processed to produce an image that is equivalent to using an ideal UWB antenna. The method is successfully tested on a breast imaging system that operates across the band from 3 GHz to 10 GHz.

Manuscript received May 29, 2013, revised September 16, 2013, accepted October 29, 2013. This work was supported by the Australian Research Council in the form of the Grant FT0991479.
The authors are with School of Information Technology and Electrical Engineering, The University of Queensland, Brisbane, QLD 4072 Australia.
E-mail: yfwang@itee.uq.edu.au

II. Synthetic Bandwidth Radar Concept

The synthetic bandwidth radar (SBR) technique refers to using a number of narrow-band antenna units to assemble an equivalent wideband antenna that cannot be realized by any conventional design method. The technique aims to synthesize several broadband antennas working separately over adjacent sub-bands to generate a UWB signal captured by a virtual equivalent antenna (VEA) working with ideal properties over the whole UWB. By using this concept, the difficulties of designing high-quality UWB antennas are alleviated as each individual antenna is optimized within a limited sub-band.

The schematic diagram of the proposed synthetic bandwidth technique is shown in Fig. 1. The whole frequency range from f_{L} to f_{H} is divided into U adjacent channels. Each channel contains an antenna unit connected to a pre-selection filter that operates within a sub-band from f_{u-1} to f_u $(u = 1,2,\ldots,\mathrm{U})$. By successively placing the U- antenna units in a specified position surrounding the target, the signals received from the antenna units $\{\boldsymbol{X}_u(\cdot)\}$ are recorded, combined and then processed by a signal integration module. The module synthesizes these signals and generates an integrated signal $\{\boldsymbol{S}(\cdot)\}$ as if it is collected from a virtual equivalent antenna (VEA) operating over the entire band. A signal integration mechanism to combine the three sub-channels is implemented during the image reconstruction process. Due to the different feeding-to-radiation delay between the antenna units, the inter-channel amplitude and phase distortions need to be compensated by a pre-test calibration procedure during the signal integration process.

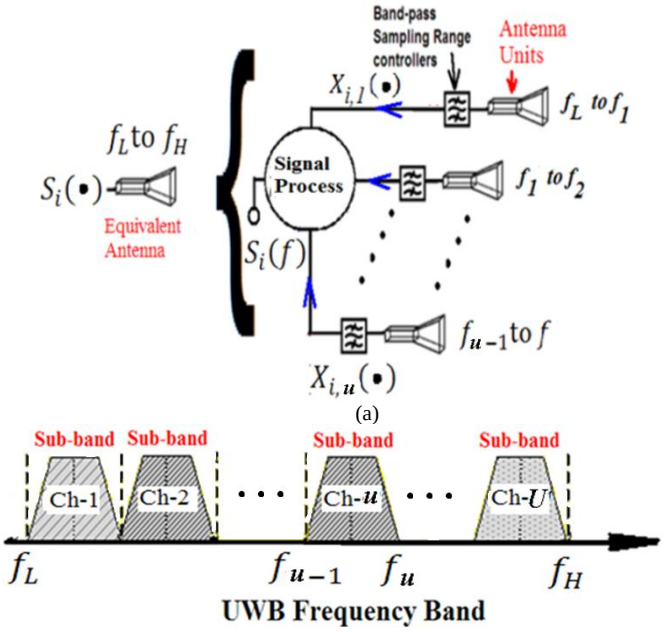

Fig. 1. (a) Bandwidth synthetic radar, and (b) system with Ψ channels.

III. Breast Imaging System Using SBR

Figure 2 shows the configuration of a UWB breast imaging system using the concept of SBR. The whole working bandwidth is divided into three sub-bands (U=3). Three sub-band antenna units (Ant-A, Ant-B, and Ant-C) surround the imaged breast with $360°/\mathrm{U} = 120°$ angular intervals. The cylindrical scanning mechanical sub-system and other hardware infrastructure employs the same developed model presented in [13]-[14]. Since no matching medium is used between the antennas and the imaged object, a proper windowed processing method is employed to cancel the effect of reflections at the skin-free-space interface. Each antenna unit directs its mainbeam towards the imaged body, whereas their phase centers are positioned at a constant distance ($\mathrm{R_{array}}$) from the central axis of the rotation table. The collected signals from the three adjacent sub-bands are connected to Channel #1 to #3 of a vector network analyzer (VNA), which is R&S ZVA24 in our case. The measured S-parameters ($\mathrm{S_{11}}, \mathrm{S_{22}}$, and $\mathrm{S_{33}}$) are stored as data for post-processing.

Figure. 3 illustrates the scan mechanism of this imaging system. Three parallel A-scans are implemented by collecting the signals from the antenna units over three sub-bands in the frequency domain. The B-scans are implemented by rotating all antenna units and extracting the signals from 3N positions evenly distributed along the circular track. The number of scanning positions is assigned as an integer multiple (N) of the number of channels (U) so that all the antennas scan the same positions around the imaged object. Thus, the phase centers of each antenna units traverse 3N positions at $\overrightarrow{a_i}$:

$$\overrightarrow{a_i} = \begin{pmatrix} R_{array}\cos\Phi_i \\ R_{array}\sin\Phi_i \end{pmatrix} \qquad where\ \Phi_i = \frac{2\pi(i-1)}{3\mathrm{N}},$$

$$i = 1,2,\ldots,3\mathrm{N}. \qquad (1)$$

The reflection coefficient measured at each scanning position ($\overrightarrow{a_i}$) by the antenna unit operating in u-channel is recorded as $\boldsymbol{X}_{i,u}$ in the vector format:

$$\boldsymbol{X}_{i,u}\left(f_m^{(u)}\right) \in \mathbb{C} \quad where\ f_m^{(u)} = f_{u-1} + (m-1)\Delta f,$$
$$\mathrm{m} = 1,2,\ldots,\mathrm{M}_u, i = 1,2,..,3\mathrm{N} \quad (2)$$

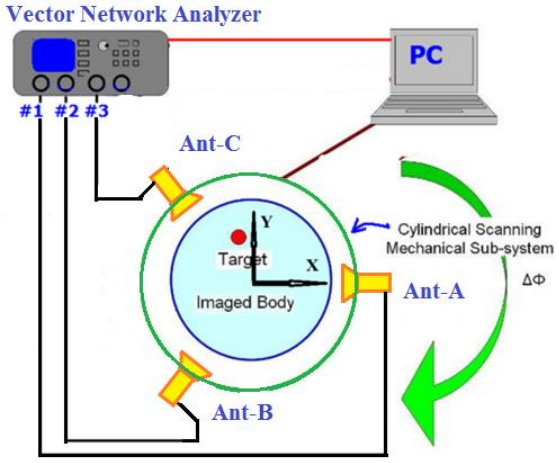

Fig. 2. UWB imaging system using synthetic bandwidth method.

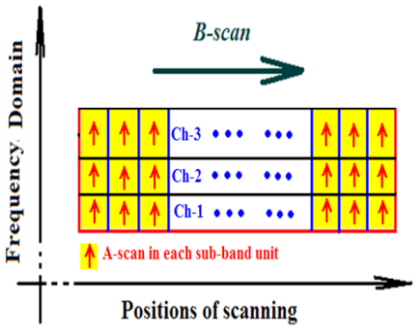

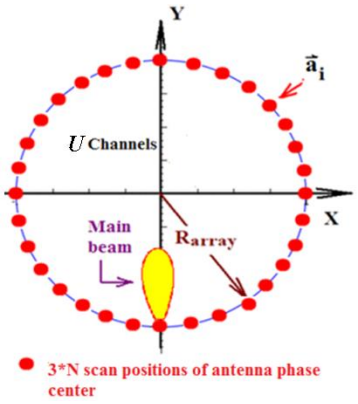

Fig. 3. (a) Scan mechanism of the system using SBR, and (b) 3N scanning positions surrounding the imaged body.

IV. Antenna Units Design

Three antenna units, Ant-A, Ant-B, and Ant-C, are designed to operate within the assigned low-, medium-, and high-sub-bands. All the sub-band antennas are designed to achieve: a) more than 20 dB return loss, b) moderate to high gain values in the mainbeam direction, c) stable radiation pattern concerning the direction of the mainbeam across the sub-band, d) flat group delay and (e) fixed phase center. Their frequency coverage and channel index are shown in Table I.

Three tapered slot antennas (TSA) are designed to meet the above requirements on the substrate Rogers RT6010LM (dielectric constant=10.2, thickness=0.64 mm). The designed Ant-B and Ant-C antennas employ a tapered slot structure on one side of the substrate and a microstrip feeder on the other side. The coupling between that feeder and the radiator is achieved using a suitable microstrip-to-slotline transition [15]. Ant-A employs an antipodal structure [16] that is connected to a partial ground on one layer and a microstrip feeder at the other layer. The physical dimensions of antennas operating at the upper channels (Ant-B and Ant-C) are further reduced by using double substrate layers covering both sides of the radiator, which is also helpful to maintain a fixed phase center according to the study in [17].

During the antennas' optimization, their time-domain behavior is given a significant emphasis. The antenna's complete behavior, including time-domain response, can be described by the linear system theory. To that end, the frequency-domain signal link suggested by the method in [8] is simulated with two identical antennas allocated face-to-face along a 180-mm distance. The transmission coefficient between the two antennas $S_{21}(f)$ is calculated and interpreted during the antenna optimization process. Based on the simulation $S_{21}(f)$ in each sub-band $(f_{u-1} < f < f_u)$, the normalized transmission loss $(TL_{Norm}^{(u)}(f))$ and relative group delay $(GD_r^{(u)}(f))$ are defined as

$$TL_{Norm}^{(u)}(f) = \left| \frac{S_{21}(f)}{\max\limits_{f\in[f_{u-1},f_u]}\{S_{21}(f)\}} \right| \qquad (3.1)$$

$$GD_r^{(u)}(f) = -\frac{d\angle S_{21}(f)}{2\pi df} - GD_{mean}^{(u)} \qquad (3.2)$$

$GD_{mean}^{(u)}(f)$ is the mean group delay created by

$$GD_{mean}^{(u)} = \frac{1}{f_u - f_{u-1}} \int_{f_{u-1}}^{f_u} [-\frac{d\angle S_{21}(f')}{2\pi df'}]df \qquad (3.3)$$

To achieve distortionless properties for all the antennas, the optimization aims to realize an even transmission loss and minimized the variations in the group delay. The optimized dimensions of the antennas and their frequency allocations are listed in Table I.

TABLE I: DESIGN PARAMETERS OF THE THREE ANTENNAS.

Antenna units	Band (GHz)	Channel index	BW (%)	Length (L) (mm)	Width (D) (mm)
Ant-A	3.0-4.5	#1	40	34	34
Ant-B	4.5-6.5	#2	36	33	27
Ant-C	6.5-10.0	#3	42	23	18
VEA	3.0-10.0	-	108	-	-

Figure 4a shows the simulated and measured reflection coefficient of the antennas. They feature a -15 dB reflection coefficient over the entire operational UWB. As depicted in Fig. 4b, the radiation pattern of each antenna demonstrates nearly frequency-independent characteristics across its sub-band. Fig. 4c illustrates that the gain of each antenna varies slightly with frequency. The gain for the three antennas varies between 2 dBi and 4 dBi. Fig. 4d shows a flat group delay in each antenna with less than 0.2 ns peak-peak variation. Figure 5 illustrates the fabricated antennas with their phase centers indicated at the narrowest part of the slot as explained in [17].

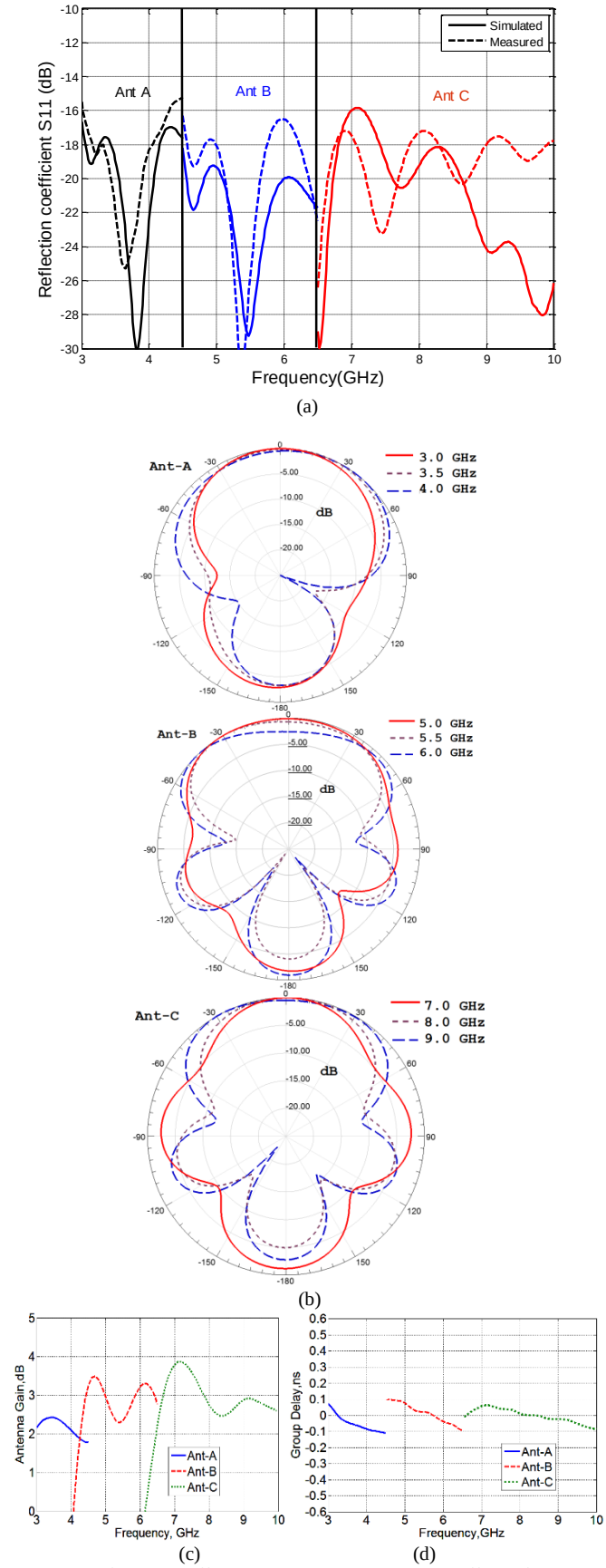

Fig. 4. (a) Reflection coefficients, (b) radiation patterns at different frequencies in the E-plane, (c) gain, and (d) group delay of the antennas.

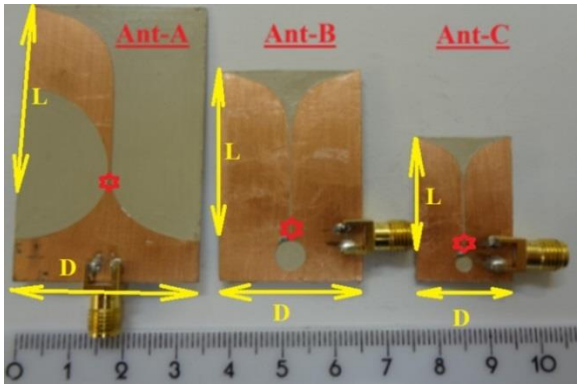

Fig. 5. Fabricated antennas. For Ant-B and Ant-C, superstrates are removed.

V. TWO-STAGE CALIBRATION

To get accurate imaging results, the phase center of each antenna should be located. Moreover, the effective permittivity of the heterogeneous imaged object in different angular directions and at all the utilized channels should be estimated. To that end, a two-stage calibration procedure is needed.

A diagram showing one of the antennas operating at channel (Ch-u) and facing an imaged body with unknown permittivity value $\varepsilon_{\text{breast}}(f)$ is depicted in Fig. 6. The phase center of that antenna is located at the point $\overrightarrow{a_i}$. The signal propagation link includes the path inside ($\vec{\xi}$ to $\vec{r}$) and outside ($\overrightarrow{a_i}$ to $\vec{\xi}$) the body. Since the conventional VNA calibration is conducted on the feeder of the antenna, the time that signal travels in the structure of the antenna unit ($\tau_{ant}^{(u)}$) needs to be separated from other timed delays for an accurate estimation of the target's position.

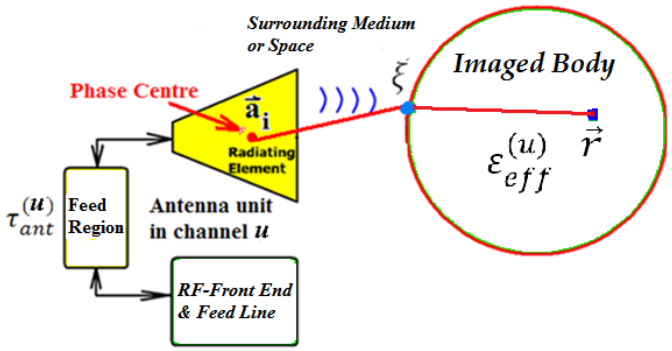

Fig. 6. Analytical model for SBR system including the structure of sub-band antenna units in each channel.

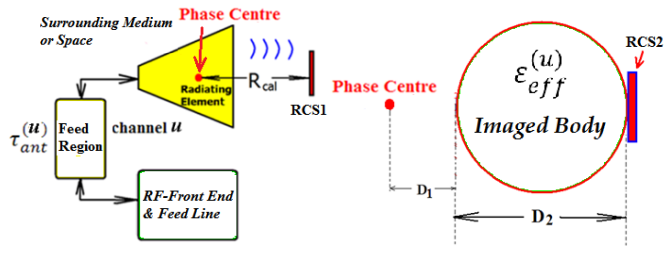

(a) (b)

Fig. 7. Two-stage calibration at each channel. (a) stage-I, (b) stage-II.

If the reference signal for the m-th step-frequency pulse is

$$Tx(t) = A_1 \cos 2\pi(f_L + m\Delta f)t \quad (4.1)$$

The reflected signal from hypothetic target after a round trip delay can be represented as

$$Rx(t) = A_2(m) \cos 2\pi(f_L + m\Delta f)[t - 2\tau_i(\vec{r}, u)] \quad (4.2)$$

where $\tau_i(\vec{r}, u)$ is the one-way-trip delay from the feeding port to the hypothetical point $\vec{r}$ in the imaged region. Its value also depends on the channel index (u) with which the reference pulse is emitted. Using the approach in [18] as well as the analysis of the feeding structure, the total one-way trip delay is

$$\tau_i(\vec{r}, u) = \tau_{ant}^{(u)} + \min_{\vec{\xi} \in \partial\Omega} \left\{ \frac{\|\overrightarrow{a_i} - \vec{\xi}\|}{c} + \frac{\|\vec{\xi} - \vec{r}\| \sqrt{\varepsilon_{eff}^{(u)}}}{c} \right\} \quad (5)$$

$\varepsilon_{eff}^{(u)}$ is the effective permittivity value of the imaged body defined by the mean group velocity (v_{mean}) over the sub-band from f_{u-1} to f_u :

$$\sqrt{\varepsilon_{eff}^{(u)}} = \left(\frac{c}{v_{mean}}\right) = (f_u - f_{u-1}) \left[\int_{f_{u-1}}^{f_u} \frac{1}{\sqrt{\varepsilon_{breast}(f)}} df \right]^{-1} \quad (6)$$

Obviously, the time-delay in (5) is not only a function of the hypothetical point position $\vec{r}$, but also depends on the channel at which the system operates. With the given hypothetical point position, the corresponding time-delay cannot be determined from (5) and (6) due to two unknown coefficients $\tau_{ant}^{(u)}$ and $\varepsilon_{avg}^{(u)}$ in each channel (u). Due to the complexity of determining these two coefficients for many factors, such as the non-straight path for the signal penetration inside the breast, the unknown delay in the feeding structure of the antenna, etc, a two-stage calibration is necessary to estimate their values.

As shown in Fig. 7, two calibrations in each channel are conducted by mounting small calibration targets at two different positions. At stage-I, the target (RCS-1) is placed in front of the antenna's aperture with a distance of R_{cal} to the antenna phase center. At stage-II, the target (RCS-1) is removed and the target (RCS-2) is inserted behind the imaged breast with ($D_1 + D_2$) distance from the phase centre. To avoid any coupling between the calibration target and antenna's body, both RCS-1 and RCS-2 are small and positioned in the far-field region of the antenna.

To get the values of the time-delays from these two-stage calibrations, the following five steps are performed on the time-domain signals that are generated in practice in the VNA using the inverse Fourier transform IFT:

1. Remove both targets RCS-1 and RCS-2 and collect the time-domain signal $S_{cal}^{0}(t)$
2. Insert target RCS-1 and collect the time-domain signal $S_{cal}^{(1)}(t)$
3. Remove target RCS-1 and then insert target RCS-2, and collect the time-domain signal $S_{cal}^{(2)}(t)$
4. Conduct the calculation:

$$\Gamma_1(t) = S_{cal}^{1}(t) - S_{cal}^{0}(t) \quad (7.1)$$

$$\Gamma_2(t) = S_{cal}^{2}(t) - S_{cal}^{0}(t) \quad (7.2)$$

$$\Gamma_1^{+}(t) = |\Gamma_1(t) + j\mathcal{H}\{\Gamma_1(t)\}| \quad (7.3)$$

$$\Gamma_2^{+}(t) = |\Gamma_2(t) + j\mathcal{H}\{\Gamma_2(t)\}| \quad (7.4)$$

$\mathcal{H}\{\cdot\}$ is the Hilbert transfer of the time-domain signal, $\Gamma_1^{+}(t)$ is the reflection from target RCS-1, and $\Gamma_2^{+}(t)$ is the reflection from target RCS-2.

5. Record the time delay τ_I where $\Gamma_1^+(\mathrm{t})$ reaches the maximum and τ_{II} where $\Gamma_2^+(\mathrm{t})$ reaches the maximum.

The estimated time-delays from these two-stage calibrations are recorded as $\tau_I^{(u)}$ and $\tau_{II}^{(u)}$ in each channel. The relations between the measured time-delay ($\tau_I^{(u)}, \tau_{II}^{(u)}$) and the two unknown coefficients ($\tau_{ant}^{(u)}, \varepsilon_{avg}^{(u)}$) are

$$\frac{1}{2}\tau_I^{(u)} = \tau_{ant}^{(u)} + \frac{R_{cal}}{c} \qquad (8.1)$$

$$\frac{1}{2}\tau_{II}^{(u)} = \tau_{ant}^{(u)} + \frac{D_1}{c} + \frac{D_2\sqrt{\varepsilon_{eff}^{(u)}}}{c} \qquad (8.2)$$

By solving these two equations, the two unknown coefficients in (5) can be determined. To accurately estimate those parameters at different angular directions, each calibration procedure is repeated at various orientations of the heterogeneous imaged breast.

VI. Imaging Reconstruction Algorithm

The value of electrical path $R_i^+(\vec{r},u)$ from an arbitrary point $\vec{r}$ to the antenna feeding port in all channels can be calculated from (5):

$$\begin{aligned} R_i^+(\vec{r},u) &= \tau_i(\vec{r},u) * c \\ &= \tau_{ant}^{(u)} * c \\ &+ \min_{\vec{\xi}\in\partial\Omega}\{\|\overrightarrow{A_i} - \vec{\xi}\| + \|\vec{\xi} - \vec{r}\|\sqrt{\varepsilon_{eff}^{(u)}}\} \end{aligned} \qquad (9)$$

The image reconstruction algorithm is developed based on the non-uniform IFT method reported in [14]. Beginning with the three-dimensional signals collected as $\boldsymbol{X}_{i,u}(f)$, the procedure for image reconstruction is

1. Find the data $\boldsymbol{X}_{i,u}(f)$ from the subtraction of adjacent-angle signals:
$$\Delta\boldsymbol{X}_{i,u}(f) = \boldsymbol{X}_{i+1,u}(f) - \boldsymbol{X}_{i,u}(f) \qquad (10)$$
2. The amplitude of the signals is normalized to compensate for the imbalance in the antenna gain in each channel:
$$\Delta\boldsymbol{X}_{i,u}^{Norm}(f) = \frac{\Delta\boldsymbol{X}_{i,u}(f)}{\max\limits_{f\in[f_{u-1},f_u]}\{|\Delta\boldsymbol{X}_{i,u}(f)|\}} \qquad (11)$$
3. Perform the calibration steps in Section V to obtain the time-delay of the antennas and the average permittivity of breast phantom in each sub-band, and establish the equation for the electrical distance $R_i^+(\vec{r},u)$.
4. Divide a square area including the cross-section of the imaged body into P×Q cells having centers at $(\mathrm{x_p}, \mathrm{y_q})$.
5. By assuming that the target is located at $\vec{r} = (\mathrm{x},\mathrm{y}) = (\mathrm{x_p}, \mathrm{y_q})$, match-filter the normalized difference signals by introducing the following correlations:
$$\Delta\boldsymbol{C}_{i,u}^{\vec{r}}(f) = \Delta\boldsymbol{X}_{i,u}^{Norm}(f)\, exp\{2jkR_i^+(\vec{r},u)\} \qquad (12)$$
6. Once the multiplied signal is correlated with frequency, Ψ channels, and Ψ ∗ N positions of circular scanning, the image can be generated:
$$\begin{aligned} &\mathrm{Imag}(\vec{r}) = \mathrm{Imag}(\mathrm{x_p}, \mathrm{y_q}) \\ &= \frac{1}{\mathrm{UN}(f_H - f_L)}\left|\sum_{i=1}^{\mathrm{U*N}}\left(\sum_{u=1}^{\mathrm{U}}\int_{f_{u-1}}^{f_u}\Delta\boldsymbol{C}_{i,u}^{\vec{r}}(f)df\right)\right| \end{aligned} \qquad (13)$$
7. Plot the calculated function $\mathrm{Imag}(\mathrm{x_p}, \mathrm{y_q})$ using various intensity colors. High probability of the presence of a target is indicated by a large value of $\mathrm{Imag}(\mathrm{x_p}, \mathrm{y_q})$.

By looking at (13), the signal integration among different sub-bands (mentioned in Section II) is implemented during the correlation calculation. The signal collected from the SBR units $\boldsymbol{X}_{i,u}(f)$ and the signal collected from the assembled VEA $\boldsymbol{S}_i(f)$ have the relation:

$$\begin{aligned} &\int_{f_L}^{f_H}\boldsymbol{S}_i(f)\, exp\{2jkR_i^{\vec{r}}\}\, df \\ &= \sum_{u=1}^{\mathrm{U}}\int_{f_{u-1}}^{f_u}\boldsymbol{X}_{i,u}^{Norm}(f)\, exp\{2jkR_i^+(\vec{r},u)\}\, df \end{aligned} \qquad (14)$$

For the signal in the format of discrete frequency sampling $\boldsymbol{X}_{i,u}(f_m^{(u)})$ in (2), (13) can be reshaped as:

$$\begin{aligned} &\mathrm{Imag}(\mathrm{x_p}, \mathrm{y_q}) \\ &= \frac{1}{U\mathrm{MN}}\left|\sum_{i=1}^{\mathrm{U*N}}\sum_{u=1}^{\mathrm{U}}\sum_{m=1}^{\mathrm{M_u}}\Delta\boldsymbol{X}_{i,u}^{Norm}\left(f_m^{(u)}\right) exp\{2jk_mR_i^+(\vec{r},u)\}\right| \end{aligned} \qquad (15)$$

It is worth mentioning that the radar ranging calculations in (5), (6) and (8) is speculated assuming an ideal geometry, which is not the accurate description of the signal transmit/scattering behavior under realistic environment, i.e. heterogeneous object that varies the phase center of the antennas in different directions slightly, with three-dimensional structure. Therefore, we noticed that using the estimated parameters ($\tau_{ant}^{(u)}, \varepsilon_{avg}^{(u)}$) produce a blurry image in some cases. To get a focused image, the estimated parameters are experimentally adjusted (≈±10%) around the estimated values in the imaging algorithm.

VII. Simulations

To validate the proposed method, simulations are conducted using a volume of a realistic breast model and the designed antennas in the full-wave simulation environment (Microwave studio CST suite 2012). As shown in Fig. 8a, the breast voxel model is imported from [19] with <25% glandular tissue and long- and short- axis of 136 mm and 96 mm, respectively (Breast ID: 071904). The breast model includes a roughly 1.5-mm-thick skin layer, and a 15-mm-thick subcutaneous fat layer at the base of the breast. The heterogeneous tissue distribution and their dispersive dielectric properties are assigned according to the measured results in [19]. An object of 10-mm diameter polyhedron representing the cancerous tumor ($\epsilon_{\mathrm{tumor}} = 45; \sigma_{\mathrm{tumor}} = 4.0\ \mathrm{S/m}$ [6]) is inserted inside the voxel model at the indicated position. Fig.8b illustrates a cross-section view of the breast volume indicating the location of the cancerous tumor. In the simulations, the volume of the breast model that includes the cancerous tumor was utilized in the computations.

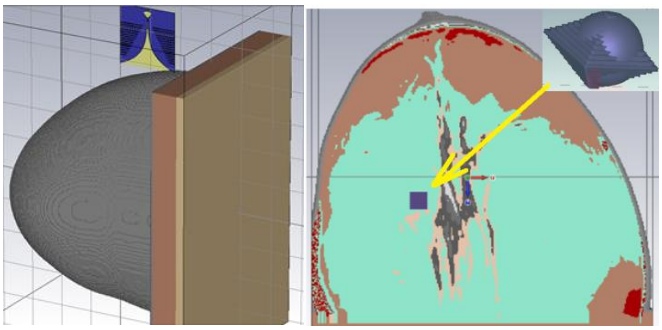

(a) (b)

Fig. 8. (a) Heterogeneous breast voxel model in simulation environment, and (b) cross-section view of the breast slice where the tumor is located.

The simulation included 3N=36 antenna positions around the imaged body in a circular track. The antennas phase centers were positioned at the same distance ($R_{array} = 110$ mm) from the central axis of the voxel model. Three different excited signals were specified for each sub-band according to the frequency allocations in Table I. The simulation was run with 3×36=108 iterations for each antenna unit at each position, and the computed signals were recorded for imaging reconstruction. To emulate the realistic situation with noise background, a Gaussian white noise was added to the signal for a 10 dB signal-to-noise ratio (SNR). To compare the proposed SBR method with the conventional method that uses one UWB antenna, the simulations were repeated but in this time, a single UWB antenna was used to capture the data. The antennas used for the comparison are tapered slot UWB antennas with band coverage of 3 GHz to 10 GHz [20], [21].

Using (9)-(15), the captured signals were processed and the images were produced. Fig. 9a-c illustrates the reconstructed images. It can be observed that proposed method produces an image with a better quality, lower clutters, and higher contrast compared with using a single UWB antenna. The lower internal clutters in the image produced using the proposed SBR method means a lower rate for the false positives than using a single UWB antenna.

To quantify the improvement in the produced image using the proposed method compared with the traditional single-antenna approach, the metrics suggested by [22] is utilized. The quality factor Q is defined as the ratio of the average intensity value of points located in the tumor region ($\mathfrak{\vartheta}$) over the points in normal breast tissue surrounded. A higher value of Q implies the tumor intensity is more intensive than the background regions.

$$Q = \frac{\mu\{Imag(\vec{p})\}}{\mu\{Imag(\vec{q})\}} \qquad (16)$$

Where $\mu\{\cdot\}$ denote the mean operation: $\forall\, \vec{p} \in \mathfrak{\vartheta}; \forall\, \vec{q} \in \bar{\bar{\mathfrak{\vartheta}}}$.

The calculated Q factor for the three images in Fig. 9 are 1.65, 1.39 and 1.43 for the SBR method, traditional method using antenna of [20] and antenna of [21], respectively. Thus, the improvement is around 15%. Of course, this improvement value increases or decreases depending on the utilized antenna and the selected region $\bar{\bar{\mathfrak{\vartheta}}}$.

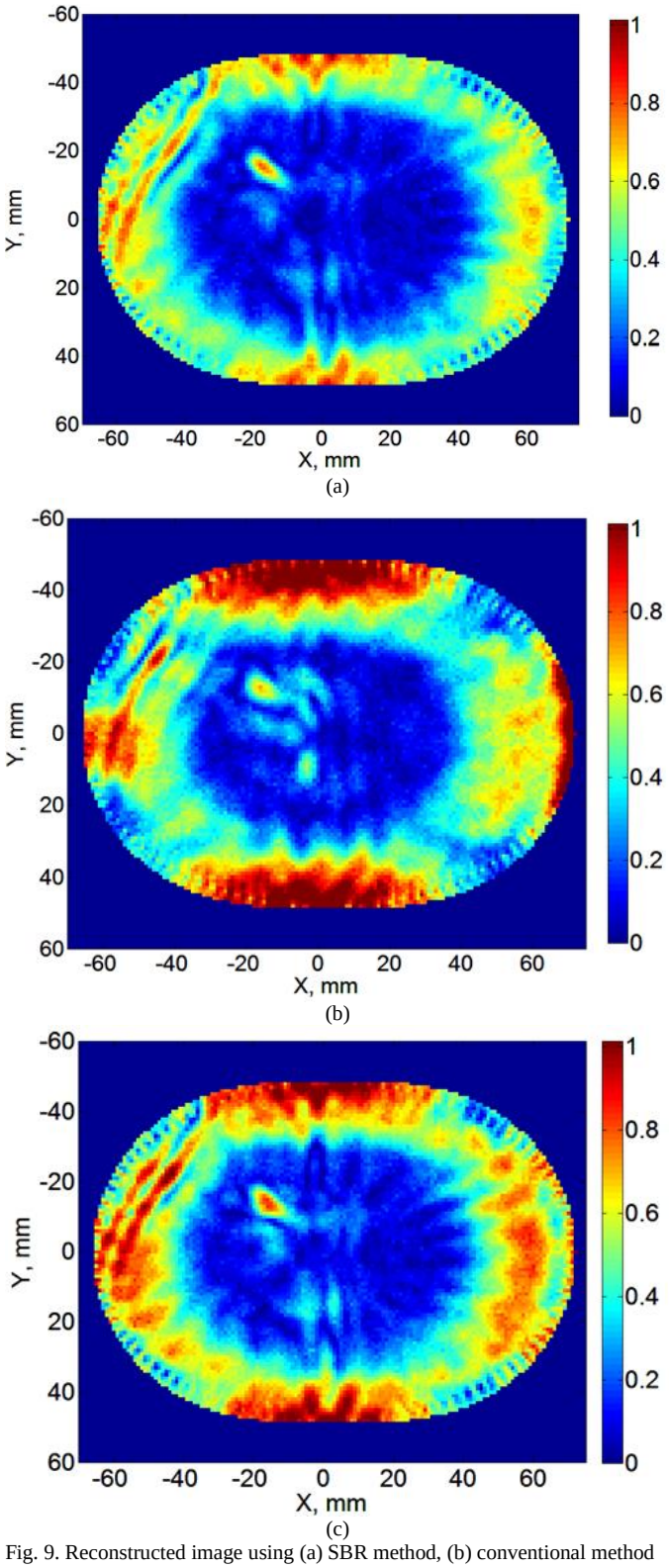

(a)

(b)

(c)

Fig. 9. Reconstructed image using (a) SBR method, (b) conventional method with corrugated TSA, and (c) conventional method with elliptical-cut TSA.

VIII. Experimental Results

To experimentally test the proposed method, an artificial heterogeneous breast phantom (diameter of 108 mm) was fabricated using a mixture of materials (water, gelatin, oil, salt and surfactant) following the procedure in [23]. The fatty tissue of the phantom has the dielectric properties ($\epsilon_b \approx 3.6; \sigma_b \approx$

0.15 S/m) that change across the frequency band (3-10 GHz) according to Debye model [24]. To emulate the heterogeneous structure, glands and other fatty types are created and distributed randomly within the phantom. Those tissues have $50-70\%$ higher permittivity values than the main fatty layer. The inserted tumor (diameter of 8 mm) has the average properties of ($\epsilon_b \approx 50; \sigma_b \approx 4.0$ S/m) at 6.5 GHz [24].

Figure 10 shows the artificial phantom installed on the developed testbed. The three fabricated antennas are installed on three mechanical arms and used to scan this phantom from 3N=36 circular positions. An experiment using 48 positions is also performed to see the effect of increasing number of scanning positions, or number of antennas, on the quality of the images. The distance between the antennas' phase center and the axis of rotation is 85 mm. A 12-mm-diameter steel ball is used for the two-stage calibration.

The reconstructed images from the experiments are shown in Fig. 11 a,c. For comparison, the images using the conventional single-antenna method covering the same total band (3-10 GHz) and employing the antenna designed according to [21] are shown in Fig. 11 b, d. Obviously, the SBR system provides a better detection and localization of the target. The detected tumor using the proposed method appears at the exact real location. However, the detected position is slightly shifted compared with the real location when using a single UWB antenna. If the images obtained using 36 scanning positions are compared with those obtained using 48 positions, it would become clear that using a large number of scanning positions results in a better quality for the image with less clutters. The improvement when using the proposed SBR method is significant as the image has one clear target which is the tumor. The clutter that appears at the left hand side of the image when using 36 scanning positions which may cause a false positive, has much less contrast in the image obtained using 48 positions. It is to be noted that the improvement in using the proposed method compared with the traditional approach is higher in the measurements (Fig. 11) than that in the simulations (Fig. 9). These results prove the robustness of the proposed method under realistic environment where not all the aspects of such an environment are under control or well-known.

IX. CONCLUSION

An ultra-wideband (UWB) imaging approach using synthetic bandwidth radar technique has been presented. Instead of designing a single UWB antenna with compromised characteristics, several antennas are designed to operate at specific sub-bands that sums to the required UWB. The design of those antennas is optimized to emulate the use of an ideal ultra-wideband antenna. A two-stage calibration method is proposed to cancel the errors associated with the change in the phase center of the antennas and to predict the average effective permittivity of the imaged object at different angular positions. Compared with the conventional imaging system using a single-antenna approach, the developed system archives better images that accurately detect the tumor and its position in a heterogeneous phantom.

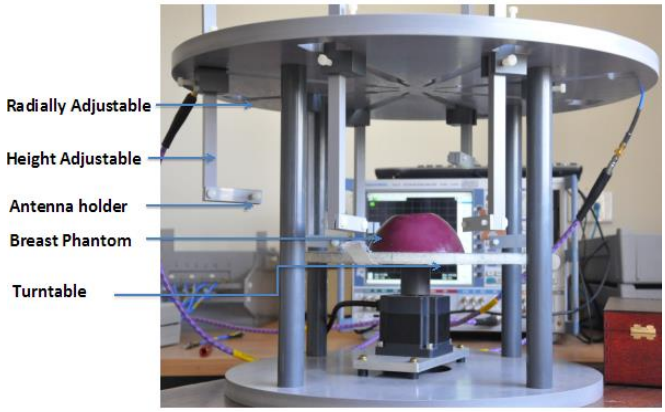

Fig. 10. Testbed for the SBR method.

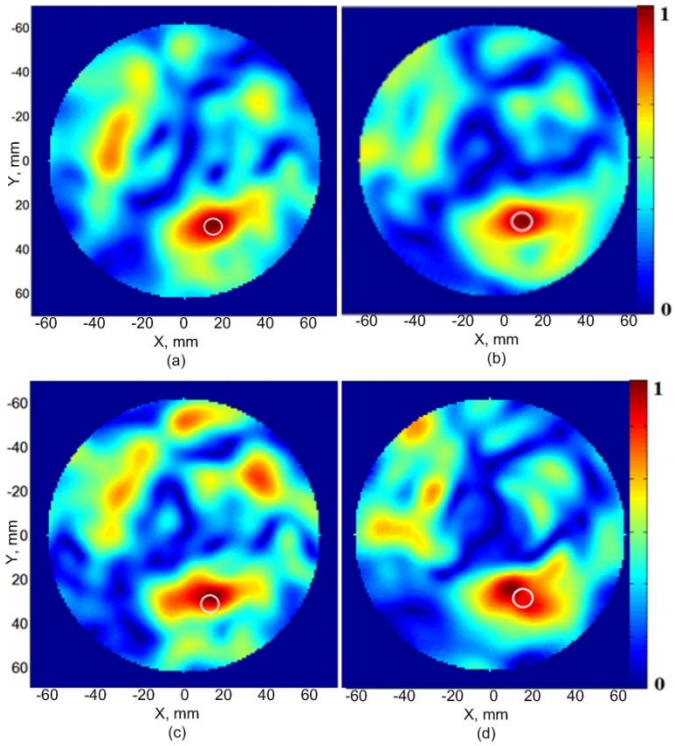

Fig. 11. Constructed image using (a) SBR method with 36 antenna positions, and (b) conventional single-UWB antenna method with 36 antenna positions(c) SBR method with 48 antenna positions, and (d) conventional single-UWB antenna method with 48 antenna positions. White circles represent the exact location of tumor.

REFERENCES

[1] D. Ireland, A. Abbosh, "Modeling human head at microwave frequencies using optimized Debye models and FDTD method," *IEEE Trans Antennas Propagat.*, vol.61, no.4, pp.2352-2355, 2013.

[2] L. Crocco, L. Di Donato, I. Catapano, T. Isernia, "An improved simple method for imaging the shape of complex targets," *IEEE Trans Antennas Propagat.*, vol.61, no.2, pp.843-851, 2013.

[3] S. Mustafa, B. Mohammed, A. Abbosh, "Novel preprocessing techniques for accurate microwave imaging of human brain," *IEEE Antennas Wireless Prop Letters*, vol.12, pp.460-463, 2013.

[4] D. Ireland, K. Bialkowski, A. Abbosh, "Microwave imaging for brain stroke detection using Born iterative method," *IET Microw Antennas Prop*, vol.7, no.11, pp.909-915, 2013

[5] Y. Chen, E. Gunawan, K. S. Low, S. Wang, Y. Kim, and C. B. Soh, "Pulse design for time reversal method as applied to ultrawideband microwave breast cancer detection: a two-dimensional analysis," *IEEE Trans Antennas Propagat.*, vol. 55, pp. 194-204, 2007.

[6] B. Mohammed, D. Ireland, A. Abbosh, "Experimental investigations into detection of breast tumour using microwave system with planar array," *IET Microw Antennas Prop*, vol.6, no.12, pp.1311-1317, 2012.

[7] J. Liang, "Study of a printed circular disc monopole antenna for UWB systems" *IEEE Trans. Antennas Propagat.*, vol. 53, pp. 3500-3504, 2005.

[8] W. Wiesbeck, G. Adamiuk, and C. Sturm. "Principles of UWB antennas basic properties and design." *Proceedings of the IEEE* vol. 97, pp. 372-385, 2009.

[9] B. Jeremie, M. Okoniewski, and E. C. Fear. "Balanced antipodal vivaldi antenna with dielectric director for near-field microwave imaging." *IEEE Trans Antennas Prop*, vol. 58, pp. 2318-2326, 2010.

[10] R. Nilavalan, I. J. Craddock, A. Preece, J. Leendertz, and R. Benjam in, "Wideband microstrip patch antenna design for breast cancer tumour detection," *IET Microwaves, Antennas Propagat*, vol. 1, no. 2, pp. 277–281, Apr. 2007.

[11] S. Hans, "The art and science of ultrawideband antennas", *Boston: Artech House*, 2005.

[12] M. S. James, "A re-examination of the fundamental limits on the radiation Q of electrically small antennas" *IEEE Trans. Antennas Propagat.*, vol. 44, pp. 672, 1996.

[13] A. Bakar, D. Ireland, A. Abbosh, and Y. Wang. "Experimental assessment of microwave diagnostic tool for ultra-Wideband breast cancer detection." *Progress in Electromagnetics Research*, *M 23* pp. 109-121, 2012.

[14] M. Bialkowski, Y. Wang, A. Bakar, and W. C. Khor. "Microwave imaging using ultra wideband frequency domain data." *Microw. Opt. Technol. Lett*, vol. 54, pp. 13-18, 2012.

[15] J. Ramakrishna, and D. Schaubert. "Analysis of the tapered slot antenna." *IEEE Transactions on Antennas and Propagation*, vol. 35, no. 9, pp. 1058-1065, 1987.

[16] A. Abbosh, H. Kan, M. Bialkowski, "Design of compact directive ultra wideband antipodal antenna," *Microw. Opt. Technol. Lett*, vol. 48, no. 12, pp. 2448-2450, 2006.

[17] S. Benoit, and A.Vorst. "Electromagnetic modes in conical transmission lines with application to the linearly tapered slot antenna." *IEEE Trans Antennas Propagat.*, vol. 48, no. 3 pp. 447-455, 2000.

[18] B. Roger, and R. Narayan, "Fermat's principle, caustics, and the classification of gravitational lens images." *The Astrophysical Journal*, pp. 310: 568-582, 1986.

[19] http://uwcem.ece.wisc.edu/MRIdatabase/InstructionManual.pdf (Online document)

[20] A. Abbosh, M. Bialkowski, "Compact directional antenna for ultra wideband microwave imaging system," *Microw. Opt. Technol. Lett*, vol. 51, no. 12, pp. 2898-2901, 2009.

[21] Y. Wang, A. Bakar, and M. Bialkowski, "Reduced-size UWB uniplanar tapered slot antennas without and with corrugations", *Microw. Opt. Technol. Lett*, vol. 53, pp. 830–836, 2010.

[22] D. Ireland, A. Abbosh, and M. Bialkowski, "Study on optimal bandwidth for microwave breast imaging" *IEEE Int Conf on Sensor Networks and Information Processing in Intelligent Sensors*, pp. 21-24, 2011.

[23] A. Bakar, A. Abbosh, P. Sharpe, M. Bialkowski, and Y. Wang, "Heterogeneous breast phantom for ultra wideband microwave imaging" *Microw. Opt. Technol. Lett*, vol. 53, pp. 1595-1598, 2011.

[24] M. Lazebnik, L. McCartney, D. Popovic, C. B. Watkins, M. J. Lindstrom, J. Harter, S. Sewall, A. Magliocco, J. H. Booske, M. Okoniewski, and S. C. Hagness, "A large-scale study of the ultrawideband microwave dielectric properties of normal breast tissue obtained from reduction surgeries," P*hysics in Medicine and Biology*, vol. 52, pp. 2637-2656, 2007.